

# Gravity's role in taming the Tayler instability in red giant cores

Domenico G. Meduri<sup>1,2</sup>, Rainer Arlt<sup>1</sup>, Alfio Bonanno<sup>1,2</sup>, and Giovanni Licciardello<sup>2</sup>

<sup>1</sup> Leibniz-Institut für Astrophysik Potsdam (AIP), An der Sternwarte 16, 14482 Potsdam, Germany

<sup>2</sup> INAF – Osservatorio Astrofisico di Catania, via S. Sofia 78, 95123 Catania, Italy

## ABSTRACT

The stability of toroidal magnetic fields within the interior of stars remains a significant unresolved issue in contemporary astrophysics. In this study, we combine a nonlocal linear analysis with 3D direct numerical simulations to examine the instability of toroidal fields within nonrotating, stably stratified stellar interiors in spherical geometry. Both analyses start from an equilibrium solution derived from balancing the Lorentz force with an anisotropic component of the fluid pressure, which is unstable to the (nonaxisymmetric) Tayler instability, and account for the combined effects of gravity and thermal diffusion. The numerical simulations incorporate finite magnetic resistivity and fluid viscosity while reaching a regime of highly stable stratification that has never been explored before. The linear analysis, which is global in the radial direction, shows that gravity significantly reduces the growth rate of the instability and uncovers the importance of unstable modes with low radial wavenumbers operating at low latitudes. The simulations trace the entire evolution of the instability from the linear to the nonlinear phase and strongly corroborate the findings of the linear analysis. Our results reveal that in highly stratified stellar interiors, the newly configured magnetic fields remain unstable only on the thermal diffusion timescale. Combining the linear analysis results with stellar evolution models of low-mass stars, we find that the limiting toroidal field strength for Tayler instability in red giant cores decreases with the stellar evolution. The predicted field strengths align with the ones expected from recent asteroseismic observations, suggesting that the observed fields may be remnants of a Tayler instability during the transition from the main sequence to the giant phase.

**Key words.** Magnetohydrodynamics (MHD) – Instabilities – Methods: numerical – Stars: interiors – Stars: magnetic field – Stars: evolution

## 1. Introduction

The origin and evolution of magnetic fields in radiative stellar interiors remain a fundamental challenge in astrophysics. Its elucidation had been compounded by the lack of direct observational constraints for any class of stellar objects until recently, when high-precision asteroseismic measurements from the Kepler mission unveiled the internal magnetic fields of red giants (Li et al. 2022). The seismic detection relies on mixed modes – oscillation modes that act as gravity modes in the core and pressure modes in the envelope of these stars – which delivered first field strength estimates of above 100 kG due to the suppression of dipolar modes attributed to magnetic fields (Fuller et al. 2015). More recently, asymmetric splittings in the mixed modes frequency spectrum were measured in 13 low-mass evolved stars, revealing strong radial fields ranging from 30 to 600 kG (Li et al. 2022, 2023; Deheuvels et al. 2023). The asteroseismic measurements probe a narrow region of the radiative cores of these stars and suggest that the radial field strength decreases from subgiants to the red giant branch, i.e. with age. These observations provide valuable constraints on the intensity of the toroidal component of the field. This breakthrough marks a new era in observational asteroseismology, driving the development of new methods for inverse problems in stellar magnetism (e.g., Bhattacharya et al. 2024), and offers an unprecedented opportunity to test and refine theoretical models of the generation and evolution of internal magnetic fields in low-mass stars.

Due to the high magnetic Reynolds number, strong toroidal magnetic fields may be expected in radiative stellar interiors. In the presence of differential rotation, even a weak poloidal field can be readily wound up into a predominantly toroidal configura-

tion. Purely toroidal fields in a radiative region can be subject to various instabilities, such as the shear-driven magnetorotational instability (Velikhov 1959; Balbus 1995) or the magnetic buoyancy instability (Parker 1966; Gilman 1970). However, in a very stably stratified fluid, it is generally accepted that the dominant instability is the one caused by electric currents maintaining the toroidal field configuration (Spruit 1999). Current-driven instabilities of pinches and torus configurations were initially studied in the context of laboratory fusion research, hence neglecting the effect of gravity (e.g., Freidberg 1970; Goedbloed & Hagebeuk 1972). In the astrophysical context, Tayler (1973) was the first to consider, in cylindrical geometry, the adiabatic stability of purely toroidal fields in a stratified, nonrotating star. The author showed that regions near the poles are always unstable to non-axisymmetric perturbations with azimuthal wavenumber  $m = 1$ . The nature of this kink-type instability, known as the Tayler instability, changes markedly when an axial field is added, even if the ratio of the axial to toroidal field strength is small (Knobloch 1992). Although it reduces the growth rate, the presence of an axial field introduces a new resonant instability of the mixed toroidal-poloidal configuration at high vertical wavenumbers, a phenomenon corroborated by numerical simulations (Bonanno & Urpin 2008b, 2011). The existence of stable equilibria for mixed toroidal-poloidal field configurations in spherical symmetry has been investigated through direct numerical simulations (Braithwaite & Nordlund 2006; Duez et al. 2010), with the most notable being the analytical solution proposed by Prendergast (1956). However, recent studies have shown that this solution is susceptible to resistive instabilities, even in the presence of strongly stable stratification, and thus cannot serve as an accurate model for magnetic fields in stars (Kaufman et al. 2022).

Stratification and rotation are known to play significant stabilizing roles on the Tayler instability of purely toroidal fields (Pitts 1985; Spruit 1999). Specifically, Bonanno & Urpin (2012) (hereafter BU12) examined the effect of stratification and finite thermal conductivity on the instability using a linear analysis in spherical geometry, adopting a global approach in the radial direction. The authors showed that while the instability growth rate  $\sigma$  can be significantly reduced, the combined effects of gravity and thermal diffusion cannot entirely suppress the instability. In the limit of highly stable stratification relevant to stellar interiors, where  $\omega_{\text{BV}} \gg \omega_{\text{A}}$ , the growth rate scales as

$$\frac{\sigma}{\omega_{\text{A}}} \sim \left( \frac{\omega_{\text{A}}}{\omega_{\text{BV}}} \right)^2, \quad (1)$$

and is associated with the fundamental eigenmode active in the equatorial region. Here,  $\omega_{\text{A}}$  is the Alfvén frequency of the background axisymmetric toroidal field, and  $\omega_{\text{BV}}$  denotes the Brunt-Väisälä frequency. Classical predictions from fully local linear analyses are often valid only near the poles of the star (e.g., Spruit 1999; Skoutnev & Beloborodov 2024) and therefore can miss the stabilizing role of gravity on the global modes substantially. To understand the dynamical role of the Tayler instability in stellar interiors, it is therefore essential to move beyond local stability analyses and conduct global studies in an appropriate spherical geometry, as demonstrated by BU12 or by Kitchatinov & Rüdiger (2008) whose disturbances are global in the latitudinal direction.

While the nonlocal analyses above provide valuable insights, they still rely on certain simplifying assumptions and cannot replace direct numerical simulations of the Tayler instability. The latter allow for the exploration of the full global character of the instability and of its nonlinear evolution. However, there are only few numerical studies of the Tayler instability in spherical geometry, and even fewer that address highly stably stratified flows. Arlt & Rüdiger (2011) and Szklarski & Arlt (2013) were the first to explore the behavior of the instability in a spherical shell to explain the magnetic fields observed at the surface of chemically peculiar intermediate-mass stars, but could reach only a limited degree of stable stratification. More recently, Guerrero et al. (2019) focused on analyzing the effect of stable stratification on the Tayler instability with simulations in a similar geometry but for an ideal flow where only thermal diffusion is taken into account. The authors found a clear suppression of the instability with increasing stratification, but the scaling (1) predicted by BU12 could not be ascertained clearly. Within the same framework, Monteiro et al. (2023) studied the combined effect of rotation and gravity. In the presence of differential rotation, Jouve et al. (2015, 2020) and Meduri et al. (2024) investigated the interplay between magnetorotational instability of predominantly toroidal fields and Tayler instability with direct numerical simulations in a spherical shell.

In this work, we present the first direct numerical simulations of the Tayler instability of a purely toroidal field in a nearly full sphere, reaching a highly stably stratified regime. In this regime, the instability growth rate follows the scaling (1), which we confirm with a new global linear analysis that generalizes the one of BU12. Unlike Guerrero et al. (2019), our numerical simulations consider a fluid with finite viscosity and magnetic diffusivity, and a more physically grounded background toroidal magnetic field where small deviations from the spherically symmetric equilibrium are attained by means of an anisotropic component of the pressure. Our linear perturbation theory and numerical results show that, in the highly stratified regime, the dynamics is

dominated by large-scale unstable modes active at low latitudes, which classical fully local approaches inevitably fail to capture.

The remainder of the present paper is organized as follows. In Sect. 2, we present a linear stability analysis of a purely toroidal field, global in radius, which generalizes the approach of BU12. We discuss the properties of the unstable eigenmodes when varying the degree of stable stratification, first in the case with no thermal diffusion and then including a finite thermal diffusivity. Section 3 presents 3D direct numerical simulations in the same spherical geometry, initialized with the same background toroidal field as the linear analysis. We investigate the stability of the relaxed axisymmetric solutions for different levels of stable stratification and compare the results with the properties of the unstable eigenmodes predicted by the linear analysis. In Sect. 4, we combine the linear perturbation theory results with stellar evolution models of low-mass stars to estimate limiting toroidal field strengths for the Tayler instability in the cores of subgiants and red giants. Finally, we compare our theoretical predictions with the recent asteroseismic measurements of the internal magnetic fields in these stars. Section 5 closes the paper with a summary of the results and key conclusions.

## 2. Global linear analysis

### 2.1. Basic equations

BU12 considered the stability of a purely axisymmetric toroidal field  $\mathbf{B} = B_\phi(r, \theta) \hat{\mathbf{e}}_\phi$  in a nonrotating stellar radiative region in spherical geometry, neglecting viscous and magnetic diffusion. The thermal diffusivity of the fluid is  $\kappa$ . Hereafter  $(r, \theta, \phi)$  denote spherical coordinates with unit vectors  $(\hat{\mathbf{e}}_r, \hat{\mathbf{e}}_\theta, \hat{\mathbf{e}}_\phi)$ . The stability analysis is global in the radial direction and local in the latitudinal and azimuthal ones.

Here we generalize this analysis by considering the latitudinal variations of the background toroidal field which were disregarded in BU12. In the latitudinal direction, our local approximation requires  $k_\theta \gg H_\theta^{-1}$ , where  $k_\theta = l/r$  is the latitudinal wavevector modulus, with  $l$  the latitudinal wavenumber, and  $H_\theta = r \partial \ln B_\phi / \partial \theta$  is the characteristic scale of the background field in the latitudinal direction. Stable stratification is considered under the Boussinesq approximation. The fluid has a uniform density  $\rho$  and therefore gravity varies linearly with radius,  $\mathbf{g} = -g(r) \hat{\mathbf{e}}_r = -g_{\text{out}} r / r_{\text{out}} \hat{\mathbf{e}}_r$ . Here  $g_{\text{out}}$  is gravity at the top of the radiative zone which is at radius  $r = r_{\text{out}}$ .

The background toroidal magnetic field varies linearly with the cylindrical radius  $\varpi$ ,

$$B_\phi = B_0 \varpi / r_{\text{out}} = B_0 r \sin \theta / r_{\text{out}}. \quad (2)$$

With this basic state, the local approximation above reads  $l \gg \cot \theta$  and therefore the analysis cannot be applied too close to the symmetry axis. The basic state explicitly satisfies the magneto-hydrostatic equilibrium

$$-\frac{\nabla P}{\rho} + \mathbf{g} + \frac{1}{\mu \rho} (\nabla \times \mathbf{B}) \times \mathbf{B} = \mathbf{0} \quad (3)$$

which is the relevant force balance in a spherical stellar interior. Here  $\mu$  is the magnetic permeability of vacuum and  $P = p(r) + h(r, \theta)$  is the sum of the hydrostatic spherically symmetric pressure  $p(r)$  that balances gravity and of a nonisotropic component  $h \propto r^2 \sin^2 \theta$  balancing the Lorentz force of the basic state. The field configuration (2) satisfies the classical instability criterion of Tayler (1973) for nonaxisymmetric perturbations with

azimuthal wavenumber  $m = 1$ ,

$$\frac{d \ln B_\phi}{d \ln \varpi} > -\frac{1}{2}, \quad (4)$$

which is valid near the symmetry axis of a nonrotating star and in the absence of diffusivities.

Following BU12, we consider small amplitude perturbations to the background fluid velocity  $\mathbf{u}$ , magnetic field  $\mathbf{B}$ , and temperature  $T$  and perform a normal mode analysis where we seek solutions of the form  $f_1(r) \exp(\sigma t - i l \theta - i m \phi)$  to the linearized MHD equations. Here  $t$  is time,  $\sigma = \sigma_R + i \sigma_I$ , and  $f_1(r)$  is a scalar function that stands for one of the components of the perturbed flow velocity  $\mathbf{u}_1$ , magnetic field  $\mathbf{B}_1$ , or temperature  $T_1$ . Linearizing the MHD equations around the basic state (3) and eliminating all variables in favor of  $u_{1r}$  and  $T_1$  as discussed in BU12, we obtain the two coupled ordinary differential equations

$$\begin{aligned} & \left[ \sigma^2 + \omega_A^2 - \frac{4\omega_A^4 \cos^2 \theta}{m^2(\sigma^2 + \omega_A^2)} \right] \frac{d^2 u_{1r}}{dr^2} \\ & + \frac{4}{r} \left[ \sigma^2 + \omega_A^2 - \frac{2il\omega_A^4 \sin \theta \cos \theta}{m^2(\sigma^2 + \omega_A^2)} - \frac{4\omega_A^4 \cos^2 \theta}{m^2(\sigma^2 + \omega_A^2)} \right] \frac{du_{1r}}{dr} \\ & + \left[ \frac{2}{r^2} \sigma - k_\perp^2 (\sigma^2 + \omega_A^2) + \frac{4\omega_A^2}{r^2} \left( \frac{k_\perp^2}{k_\phi^2} - \frac{k_\theta^2}{k_\phi^2} \frac{\sigma^2}{\sigma^2 + \omega_A^2} \right. \right. \\ & \left. \left. - \frac{2\omega_A^2 \cos^2 \theta}{m^2(\sigma^2 + \omega_A^2)} - \frac{3il\omega_A^2 \sin \theta \cos \theta}{m^2(\sigma^2 + \omega_A^2)} \right) \right] u_{1r} = -k_\perp^2 \alpha g \sigma T_1, \end{aligned} \quad (5)$$

$$\frac{d}{dr} \left[ \kappa^2 \frac{dT_1}{dr} \right] - (\sigma + \kappa k_\perp^2) T_1 = \frac{\omega_{\text{BV}}^2}{\alpha g_{\text{out}}} u_{1r}. \quad (6)$$

In the equations above, the Alfvén frequency of the background azimuthal field is

$$\omega_A = \frac{B_\phi k_\phi}{(\mu\rho)^{1/2}}, \quad (7)$$

$\omega_{\text{BV}}$  is the Brunt-Väisälä frequency defined by

$$\omega_{\text{BV}}^2 = -g_{\text{out}} \alpha (\nabla_{\text{ad}} T - \nabla T) \cdot \hat{e}_r, \quad (8)$$

where  $\alpha$  is the thermal expansion coefficient,  $k_\perp = k_\theta^2 + k_\phi^2$ , and  $k_\phi = m/r \sin \theta$  is the azimuthal wavevector modulus. The adiabatic temperature gradient is  $\nabla_{\text{ad}} T$  and the actual temperature gradient is subadiabatic,  $\nabla T > \nabla_{\text{ad}} T$ . The perturbed magnetic field  $\mathbf{B}_1$  is obtained from the velocity perturbations through the linearized induction equation

$$\frac{\partial \mathbf{B}_1}{\partial t} = \nabla \times (\mathbf{u}_1 \times \mathbf{B}). \quad (9)$$

In the limit of large radial wavenumbers,  $k_r \gg k_\theta$ , our analysis is consistent with a purely local approach as expected. Considering the radial part of the perturbations as  $f_1 = e^{-ik_r r}$  and keeping only terms of  $O(k_r^{-1})$  in Eqs. (5) and (6), we obtain the dispersion relation

$$\left( \sigma^2 + \omega_A^2 + \frac{k_\perp^2}{k_r^2} \omega_{\text{BV}}^2 \frac{\sigma}{\sigma + \kappa k_r^2} \right) (\sigma^2 + \omega_A^2) - 4 \frac{\omega_A^4}{m^2} \cos^2 \theta = 0. \quad (10)$$

This dispersion relation is identical to the one obtained by the local analysis of Skoutnev & Beloborodov (2024) when considering our background toroidal field.

As we shall see in the following, our global analysis provides a fresh perspective on the influence of gravity on the Tayler instability in spherical geometry. Notably, it elucidates the dynamical role of the different unstable eigenmodes, addressing key limitations inherent in classical fully local approaches.

## 2.2. Numerical results

To nondimensionalize the linear equations above we use the outer boundary radius  $r_{\text{out}}$  as reference length scale and the characteristic Alfvén travel time  $t_A = 1/\omega_{A0}$  as reference timescale, where

$$\omega_{A0} = \frac{B_0}{(\mu\rho)^{1/2} r_{\text{out}}} \quad (11)$$

is the Alfvén frequency based on the background toroidal field at the equator on the outer boundary,  $B_0$ . The dimensionless radius, radial velocity perturbation, and temperature perturbation are  $\tilde{r} = r/r_{\text{out}}$ ,  $\tilde{u}_{1r} = u_{1r} \omega_{A0} / \alpha T_0 g_{\text{out}}$ , and  $\tilde{T}_1 = T_1 / \delta^2 T_0$ , respectively. Here  $T_0$  is a reference temperature for the background temperature gradient  $(\nabla T - \nabla_{\text{ad}} T) \cdot \hat{e}_r = 0.01 (\tilde{r}^{-2} - 1) T_0 / r_{\text{out}}$  which is set by the boundary conditions. In this scaling scheme, Eqs. (5) and (6) read

$$\begin{aligned} & \left[ \Gamma^2 + m^2 - \frac{4m^2 \cos^2 \theta}{\Gamma^2 + m^2} \right] \frac{d^2 \tilde{u}_{1r}}{d\tilde{r}^2} \\ & + \frac{4}{\tilde{r}} \left[ \Gamma^2 + m^2 - \frac{2ilm^2 \sin \theta \cos \theta}{\Gamma^2 + m^2} - \frac{4m^2 \cos^2 \theta}{\Gamma^2 + m^2} \right] \frac{d\tilde{u}_{1r}}{d\tilde{r}} \\ & + \left\{ \frac{2}{\tilde{r}^2} \Gamma - \left( \frac{l^2}{\tilde{r}^2} + \frac{m^2}{\tilde{r}^2 \sin^2 \theta} \right) (\Gamma^2 + m^2) \right. \\ & \left. + \frac{4m^2}{\tilde{r}^2} \left[ \left( \frac{l^2 \sin^2 \theta}{m^2} + 1 \right) - \frac{l^2 \sin^2 \theta}{m^2} \frac{\Gamma^2}{\Gamma^2 + m^2} - \frac{2 \cos^2 \theta}{\Gamma^2 + m^2} \right. \right. \\ & \left. \left. - \frac{3il \sin \theta \cos \theta}{\Gamma^2 + m^2} \right] \right\} \tilde{u}_{1r} = - \left( \frac{l^2}{\tilde{r}^2} + \frac{m^2}{\tilde{r}^2 \sin^2 \theta} \right) \Gamma \tilde{g} \delta^2 \tilde{T}_1, \end{aligned} \quad (12)$$

$$\frac{d}{d\tilde{r}} \left[ \epsilon^2 \frac{d\tilde{T}_1}{d\tilde{r}} \right] - \left[ \Gamma + \epsilon \left( \frac{l^2}{\tilde{r}^2} + \frac{m^2}{\tilde{r}^2 \sin^2 \theta} \right) \right] \tilde{T}_1 = \tilde{\omega}_{\text{BV}}^2 \tilde{u}_{1r}, \quad (13)$$

where  $\tilde{g} = \tilde{r}$  is the dimensionless gravitational acceleration and  $\Gamma = \sigma / \omega_{A0}$ . Here, we defined  $\omega_{\text{BV}} = \omega_{\text{BV}0} \tilde{\omega}_{\text{BV}}(\tilde{r})$ , where  $\omega_{\text{BV}0} = \alpha T_0 g_{\text{out}} / r_{\text{out}}$ . In the equations above, two dimensionless parameters characterize the ratios among the three relevant timescales of the problem: the stratification parameter

$$\delta = \frac{\omega_{\text{BV}0}}{\omega_{A0}} \quad (14)$$

and the ratio of the thermal diffusion rate  $\omega_T = \kappa / r_{\text{out}}^2$  to the Alfvén frequency,

$$\epsilon = \frac{\omega_T}{\omega_{A0}}. \quad (15)$$

In radiative stellar interiors, the Brunt-Väisälä frequency is the largest of all frequencies, reflecting strong stable stratification. The thermal diffusivity  $\kappa$  is generally much larger than the fluid viscosity and magnetic diffusivity, which motivates our initial simplifying assumption of inviscid and perfectly electrically conducting fluid. If the toroidal magnetic field is not very weak, we therefore expect the following ordering of timescales

$$\omega_{\text{BV}0} \gg \omega_{A0} \gg \omega_T \quad (16)$$

or, in terms of dimensionless parameters,

$$\epsilon \ll 1 \ll \delta. \quad (17)$$

To prevent singularities at the center, we introduce a small inner core of radius  $\tilde{r}_{\text{in}} = r_{\text{in}} / r_{\text{out}} = 0.1$ . We employ impenetrable flow boundary conditions, that is  $\tilde{u}_{1r} = 0$  at  $\tilde{r}_{\text{in}} = 0.1$  and  $\tilde{r}_{\text{out}} = 1$ . The temperature perturbations  $\tilde{T}_1$  are zero at both boundaries.

**Table 1.** Normalized growth rates of the most unstable eigenmodes  $B_{1\theta}$ ,  $\Gamma_{\max} = \sigma_{\max}/\omega_{A0}$ , for different values of the stratification parameter  $\delta$ . For each value of  $\epsilon$ , high latitude ( $\theta = 5^\circ$ ) and equatorial ( $\theta = 90^\circ$ ) locations are listed. The growth rates for  $\epsilon = 10^{-2}$  and  $\theta = 90^\circ$  are presented for the localized and distributed eigenmodes, with the latter ones given in parentheses. The radial wavenumbers  $k_r$  in the last two columns correspond to the peak values of the Fourier power spectrum and are expressed in units of the radial domain length scale,  $D = r_{\text{out}} - r_{\text{in}}$ .

$\delta$	$\epsilon = 0$		$\epsilon = 10^{-2}$				
	$\Gamma_{\max}$		$\theta = 5^\circ$	$\Gamma_{\max}$		$k_r D$	
	$\theta = 5^\circ$	$\theta = 90^\circ$		$\theta = 90^\circ$	$\theta = 5^\circ$	$\theta = 90^\circ$	
0	1.00	0.99	1.00	0.99 (0.65)	54	2 (8)	
5	1.00	0.81	1.00	0.98 (0.59)	54	2 (8)	
10	1.00	0.58	1.00	0.94 (0.50)	54	3 (8)	
50	1.00	stable	1.00	0.54 (0.41)	46	10 (1)	
500	0.99	stable	1.00	0.012 (0.006)	51	15 (3)	

Equations (12) and (13), along with the boundary conditions above, define a nonlinear eigenvalue problem which we solve numerically using an eight-order centered finite differences scheme. We typically use a radial grid with 500 points, which, as we generally verified, ensures convergence of the numerical results. Hereafter we fix the latitudinal wavenumber to  $l = 10$  and  $\epsilon$  to  $10^{-2}$ . For this choice of  $l$ , the local approximation used in our analysis is not strictly valid for colatitudes  $\theta \lesssim 5^\circ$ . However, we find no significant variation in the results when considering  $\theta = 5^\circ$  and a higher value of  $10^\circ$  where the local approximation remains fulfilled.

Instability occurs when  $\Gamma_R$ , the real part of  $\Gamma$ , is positive. For simplicity of notation, we set  $\Gamma_R = \Gamma$  and omit the superscript  $\sim$  for nondimensional quantities henceforth. Note that the coefficients of the linear equations depend on the colatitude  $\theta$ , causing the growth rate to also vary with this quantity,  $\Gamma = \Gamma(\theta)$ . We confirmed that instability occurs for an azimuthal wavenumber  $m = 1$ , while  $m = 0$  and  $m > 1$  remain stable, as expected for the chosen background field configuration. The next two sections examine the behavior of this nonaxisymmetric,  $m = 1$  instability under increasing stable stratification varying  $\delta$  from 0 to  $10^3$ , first neglecting thermal diffusion and subsequently incorporating its effects.

### 2.2.1. Diffusionless case

We first discuss the case when the thermal diffusivity is zero, that is  $\epsilon = 0$ . Figure 1a presents the radial profiles of the most unstable eigenmodes  $B_{1\theta}(r)$  at high latitudes ( $\theta = 5^\circ$ ) for different values of the stratification parameter  $\delta$ . The growth rates  $\Gamma_{\max}$  of these eigenmodes are always of about  $\omega_{A0}$  as expected for the Tayler instability. In the unstratified case ( $\delta = 0$ ), the most unstable eigenmode covers a large portion of the outer radial domain (black line). When considering a weak stable stratification of  $\delta = 5$ , the eigenmode significantly shifts towards larger radii (blue line). For  $\delta \geq 10$ , the eigenmodes progressively concentrate towards the polar region where the influence of stable stratification is less pronounced: the unstable motions, which occur in the cylindrical radial direction  $\hat{e}_r$ , are perpendicular to the stabilizing buoyancy force in this region. In the limit of very high stratification, only a region arbitrarily close to the pole is unstable (red line in Fig. 1a), as expected from classical local linear analysis results in cylindrical geometry, which are valid near the symmetry axis (Acheson & Gibbons 1978; Spruit 1999).

When moving away from the symmetry axis towards lower latitudes, the component of the buoyancy force in the cylindrical radial direction progressively increases, reaching its maximum at the equator where is antiparallel to the direction of the unsta-

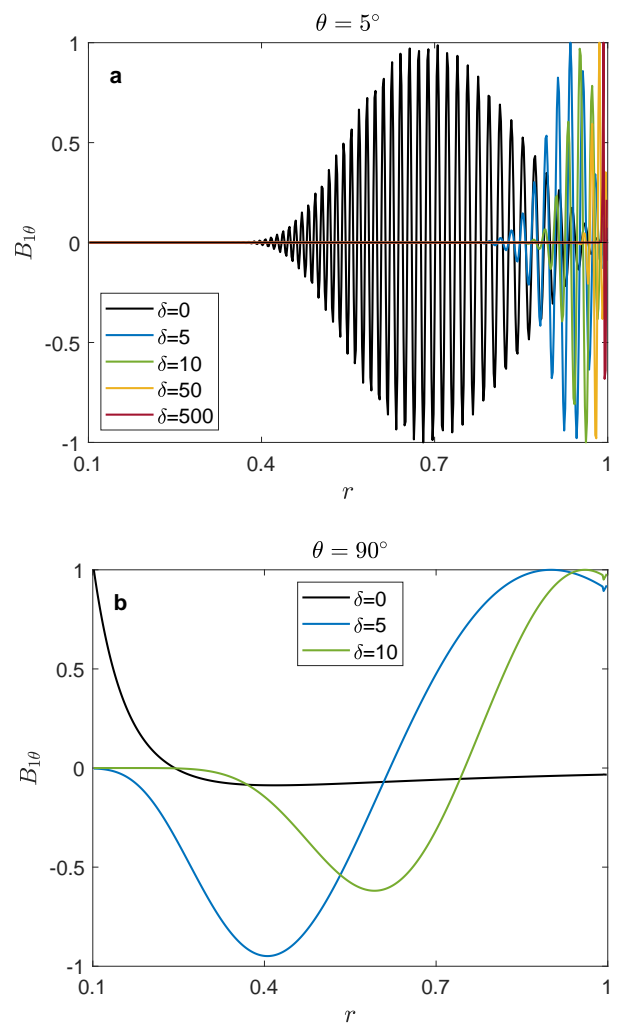


**Fig. 1.** Radial profiles of the most unstable eigenmodes  $B_{1\theta}$  for different values of the stratification parameter  $\delta$  (see the legend insets) at colatitudes (a)  $\theta = 5^\circ$  and (b)  $\theta = 90^\circ$ . No thermal diffusivity is considered ( $\epsilon = 0$ ). The growth rates  $\Gamma_{\max}(\theta = 5^\circ)$  are of about the Alfvén frequency of the background toroidal field  $\omega_{A0}$ , while they are generally lower at the equator (see the second and third column of Table 1). At the equator, there is no unstable eigenmode for  $\delta \geq 20$ .

ble motions  $\hat{e}_r$ . At the equator, we indeed find that there is no instability for  $\delta \geq 20$ . Such a geometrical effect on the stabilizing role of gravity in a sphere was already noted by Goossens & Taylor (1980) in their diffusionless stability analysis. For  $\delta < 20$ ,

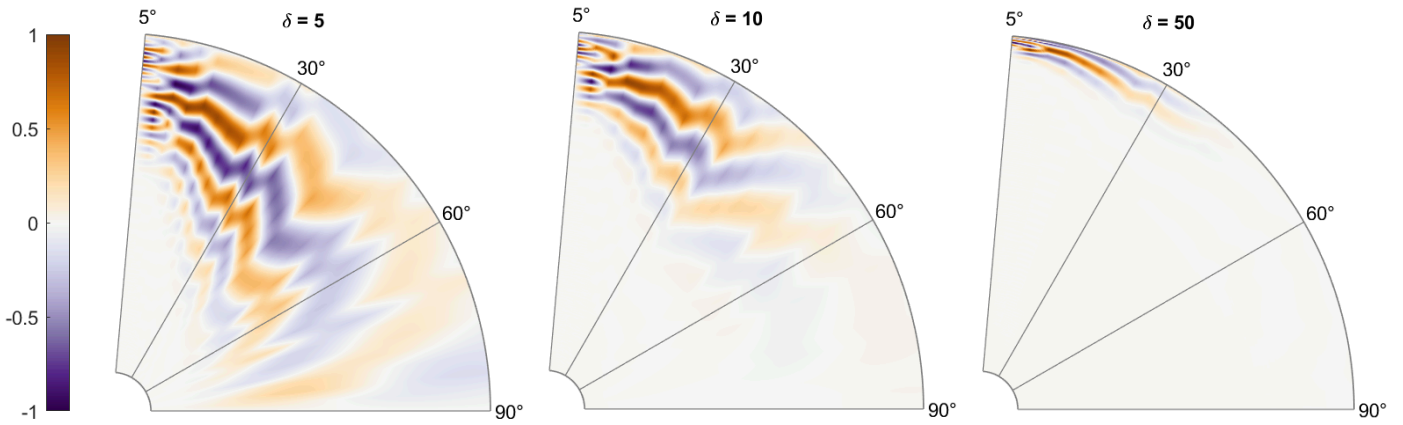


**Fig. 2.** Meridional plane reconstructions of the unstable latitudinal field perturbations,  $B_{1\theta} \exp(\Gamma_{\max} t - i l \theta)$ , for the diffusionless case ( $\epsilon = 0$ ). Here time  $t$  is  $10 \omega_{A0}^{-1}$  and the latitudinal wavenumber is  $l = 10$ . The eigenmodes are assumed to grow in phase at all latitudes. From left to right, the stratification parameter  $\delta$  is 5, 10, and 50 respectively.

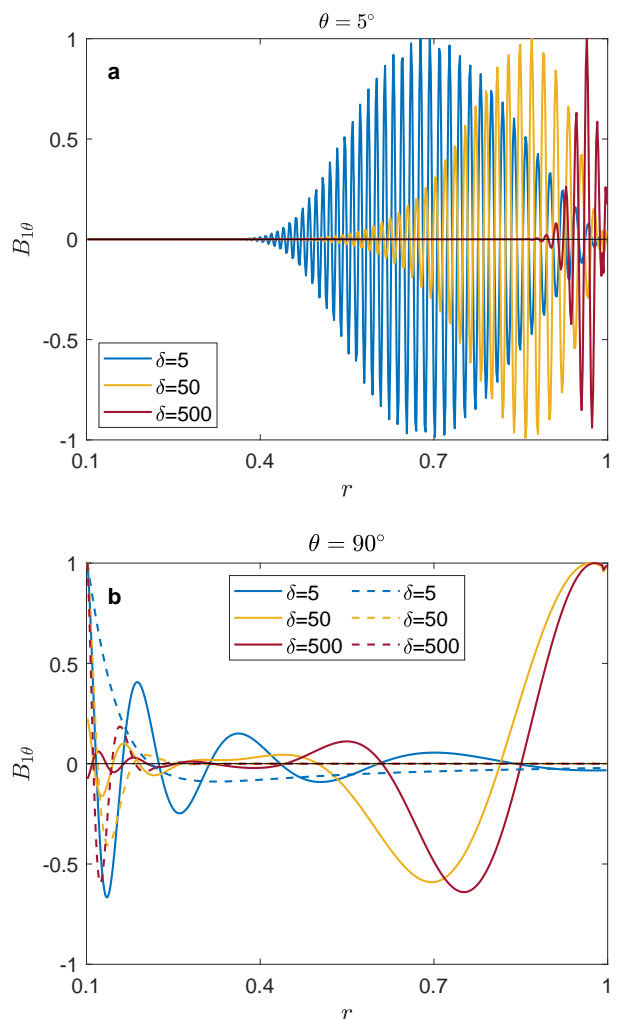
stratification is not so strong and instability exists. The maximum growth rates obtained in the equatorial region are lower than the adiabatic ones found at high latitudes with  $\Gamma_{\max} \approx 0.6$  at  $\delta = 10$ . In contrast to the ones at high latitude, the equatorial eigenmodes are characterized by only a few nodes in the radial direction, as shown in Fig. 1b.

Figure 2 displays the structure of the unstable latitudinal field perturbations in half of the meridional plane, that is  $B_{1\theta} \exp(\Gamma_{\max} t - i l \theta)$ , for  $\delta = 5, 10, \text{ and } 50$ . Here time is  $t = 10 \omega_{A0}^{-1}$  and we assumed that the perturbations grow in phase at each colatitude. As discussed above, the instability becomes confined towards the poles as stratification increases. We also find that the characteristic radial length scale of the instability decreases with increasing  $\delta$ , and that the unstable fluctuations become progressively more aligned along equipotential surfaces.

## 2.2.2. Effect of thermal diffusivity

We now discuss the effect of thermal diffusivity ( $\epsilon > 0$ ) on the instability. Thermal diffusion can reduce the effect of the stabilizing buoyancy force by dampening the amplitude of the temperature perturbations that enter the buoyancy force on the right hand side of Eq. (12), significantly changing the structure of the unstable eigenmodes and their growth rates.

At a high latitude of  $\theta = 5^\circ$ , as observed in the diffusionless case, the most unstable eigenmodes  $B_{1\theta}$  progressively concentrate towards the poles as stratification increases (Fig. 3a). However, since thermal diffusion limits the effect of stable stratification, the eigenmodes cover, for a given value of  $\delta$ , larger portions of the radial domain (cf. the cases at  $\delta = 5$  and 50 in Fig. 3a and Fig. 1a). Only for  $\delta = 500$  we observe a similar confinement of the eigenmodes in the polar region as the one obtained for  $\delta = 50$  in the diffusionless case. The growth rates of the most unstable eigenmodes are  $\Gamma_{\max} \approx \omega_{A0}$  for all values of  $\delta$  explored here. Figure 3a shows that the characteristic radial length scale of the eigenmodes does not vary significantly with stratification. A Fourier analysis of these radial profiles reveals that the power spectrum peaks at a radial wavenumber  $k_r \approx 50/D$ , where  $D = r_{\text{out}} - r_{\text{in}}$  is the radial domain length scale (Table 1). We note, however, that eigenmodes with larger characteristic radial wavenumbers are also unstable, with growth rates comparable to those presented here. This result confirms previous findings obtained for a similar background field configuration in cylin-



**Fig. 3.** Same as Fig. 1 but for  $\epsilon = 10^{-2}$ . The solid and dashed lines in (b) refer to the distributed and localized eigenmodes respectively. The growth rates of all eigenmodes are reported in Table 1.

drical geometry, which remain applicable near the poles in our spherical geometry (Bonanno & Urpin 2008a).

Moving towards lower latitudes, due to the geometrical reasons discussed before, the effect of stable stratification on the

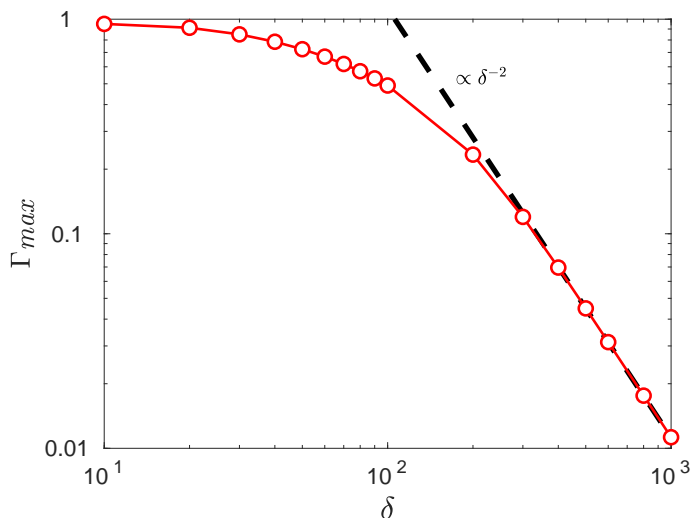


**Fig. 4.** Dimensionless growth rates of the most unstable distributed equatorial eigenmodes,  $\Gamma_{\max}$ , as a function of the stratification parameter  $\delta$  for  $\epsilon = 10^{-2}$ . The dashed line illustrates the scaling  $\Gamma_{\max} \propto \delta^{-2}$  predicted by BU12.

unstable motions increases, being maximum at the equator. In the equatorial region, larger growth rates are associated with two types of eigenmodes. The most unstable ones are characterized by radial profiles localized near the inner boundary of the fluid domain (dashed lines in Fig. 3b) with typical radial wavenumbers of  $k_r \approx 15/D$  in the most stratified cases with  $\delta \geq 500$  explored here. The second type of eigenmodes, which are reminiscent of those reported by BU12, have lower growth rates than the localized ones but are distributed throughout the fluid domain, with only a few nodes along the radial direction (solid lines in Fig. 3b; see Table 1 for their growth rates and radial wavenumbers). The growth rates of both types of these low-latitude eigenmodes decrease as stratification increases, reaching values as small as  $\sim 10^{-2} \omega_{A0}$  in the most stratified case of  $\delta = 10^3$  that we explore here.

Figure 4 presents the dimensionless growth rate of the most unstable distributed equatorial eigenmodes,  $\Gamma_{\max}(\theta = 90^\circ)$ , as a function of the stratification parameter  $\delta$ . For weak up to moderate stratification values of  $\delta = 200$ , the growth rate slowly decreases as stratification increases, but always remaining of the order of the background Alfvén frequency  $\omega_{A0}$ . In the highly stratified regime  $\delta > 200$ , the growth rate decreases more steeply, following the scaling

$$\Gamma_{\max} \propto \delta^{-2} \quad (18)$$

already predicted by BU12 (dashed line).

Unlike classical fully local approaches, our linear analysis successfully captures the global radial properties of the instability. To extend the analysis beyond the local approximation in latitude, we now turn to self-consistent direct numerical simulations, presented in the next section.

### 3. Direct numerical simulations

#### 3.1. Governing equations

As in the global linear analysis above, we consider a MHD fluid confined to a wide-gap spherical shell of aspect ratio  $\chi = r_{\text{in}}/r_{\text{out}} = 0.1$ , where  $r_{\text{in}}$  and  $r_{\text{out}}$  are the inner and outer boundary radii respectively. The fluid has uniform density  $\rho$ , gravity varies

linearly with radius,  $\mathbf{g} = -g(r)\hat{\mathbf{e}}_r = -g_{\text{out}}r/r_{\text{out}}\hat{\mathbf{e}}_r$ , and stable stratification is considered under the Boussinesq approximation as in the linear analysis. Differently from the linear analysis, we consider a viscous fluid with finite electrical conductivity, characterized by the kinematic viscosity  $\nu$  and the magnetic diffusivity  $\eta$ . The thermal diffusivity of the fluid is  $\kappa$ . We employ the mid-shell radius  $r_0 = r_{\text{in}} + D/2$  as reference length scale and the magnetic diffusion time  $r_0^2/\eta$  as reference timescale. Here  $D = r_{\text{out}} - r_{\text{in}}$  is the spherical shell gap. The magnetic field is scaled in units of  $(\mu\rho)^{1/2}\eta/r_0$ , hence the dimensionless magnetic field coincides with the Lundquist number

$$\text{Lu} = \frac{B^* r_0}{(\mu\rho)^{1/2}\eta}. \quad (19)$$

The fluid velocity is expressed in units of  $\eta/r_0$  and the scale for temperature is  $\Delta T = T_{\text{out}} - T_{\text{in}} > 0$ , the imposed background temperature contrast between the isothermal outer and inner boundaries that establishes stable stratification. The non-hydrostatic pressure  $\Pi$  is scaled with  $\rho\eta^2/r_0^2$ . In this scaling scheme, the dimensionless equations governing the evolution of the fluid velocity  $\mathbf{u}$ , the magnetic field  $\mathbf{B}$ , and the temperature perturbations  $\vartheta$  around the background temperature  $T_c$  are:

$$\frac{\partial \mathbf{u}}{\partial t} + (\mathbf{u} \cdot \nabla)\mathbf{u} = -\nabla\Pi + \delta_0^2 \text{Lu}_0^2 \frac{r}{r_{\text{out}}} \vartheta \hat{\mathbf{e}}_r + \text{Pm}\nabla^2 \mathbf{u} + (\nabla \times \mathbf{B}) \times \mathbf{B}, \quad (20)$$

$$\frac{\partial \mathbf{B}}{\partial t} = \nabla \times (\mathbf{u} \times \mathbf{B}) + \nabla^2 \mathbf{B}, \quad (21)$$

$$\frac{\partial \vartheta}{\partial t} + (\mathbf{u} \cdot \nabla)\vartheta + (\mathbf{u} \cdot \nabla)T_c = \frac{\text{Pm}}{\text{Pr}} \nabla^2 \vartheta. \quad (22)$$

The flow and the magnetic field obey solenoidality,

$$\nabla \cdot \mathbf{u} = 0 \quad \text{and} \quad \nabla \cdot \mathbf{B} = 0. \quad (23)$$

The background temperature  $T_c$  is the solution to the heat conduction equation  $\nabla^2 T = 0$ , which is

$$T_c(r) = a/r + b, \quad (24)$$

where  $a = 2\chi/(\chi + 1)^2$  and  $b = 1 + (1 + \chi)^{-1}$  for the imposed temperature boundary values of  $T_{\text{in}}/\Delta T$  and  $T_{\text{out}}/\Delta T$ . The Brunt-Väisälä frequency  $N$  is related to this temperature profile by

$$N^2(r) = g\alpha \frac{dT_c}{dr}, \quad (25)$$

where  $\alpha$  is the coefficient of thermal expansion. We define a reference value for the Brunt-Väisälä frequency,  $N_0$ , as

$$N_0^2 = g_{\text{out}}\alpha \frac{\Delta T}{r_0}. \quad (26)$$

We impose impenetrable, stress-free boundary conditions for the flow and perfect conductor conditions for the magnetic field at both spherical boundaries  $r = r_{\text{in}}$  and  $r = r_{\text{out}}$ .

In Eqs. (20)–(22), there are four dimensionless control parameters. The first is the stratification parameter

$$\delta_0 = \frac{N_0}{\omega_{A0}}, \quad (27)$$

where  $\omega_{A0} = B_0^*/(\mu\rho)^{1/2}r_0$  is the Alfvén frequency based on the initial magnetic field strength  $B_0^*$  that will be defined below (note that this definition differs from Eq. (11), which is the one used throughout Sect. 2). The second parameter is the initial



**Table 2.** Input stratification parameter  $\delta_0$  and output diagnostics of the numerical simulation runs. In all runs, the initial Lundquist number and the magnetic Prandtl number are  $\text{Lu}_0 = 2455$  and  $\text{Pm} = 1$  respectively. In the stratified runs ( $\delta_0 > 0$ ), the Prandtl number is  $\text{Pr} = 10^{-2}$ .

Name	$\delta_0$	$t_1 \omega_{A0}$	$\bar{\delta}_1$	$\bar{\text{Lu}}_1$	$\sigma/\bar{\omega}_{A1}$
TU0	0	26.6	0	677	1.09
TS1	8	24.3	3.5	681	0.94
TS2	63	24.2	27	682	0.77
TS3	126	26.0	54	680	0.60
TS4	209	25.2	90	681	0.43
TS5	300	26.9	130	678	0.28
TS6	419	24.5	180	682	0.16
TS7	628	27.7	272	678	0.07
TS8	900	27.3	321	678	0.04

Lundquist number  $\text{Lu}_0 = B_0^* r_0 / (\mu \rho)^{1/2} \eta$ . The last two parameters are the Prandtl number

$$\text{Pr} = \frac{\nu}{\kappa} \quad (28)$$

and the magnetic Prandtl number

$$\text{Pm} = \frac{\nu}{\eta}. \quad (29)$$

To solve the problem above, we employ the open-source pseudo-spectral MHD code MagIC (Wicht 2002; Schaeffer 2013). The numerical method is described in detail in Christensen & Wicht (2007) and we therefore mention only the essentials here. The code uses a poloidal-toroidal decomposition of the vector fields  $\mathbf{u}$  and  $\mathbf{B}$ . The associated poloidal and toroidal potentials, along with the temperature, are expanded using spherical harmonic functions in the latitudinal and azimuthal directions. In the radial direction, a Chebyshev collocation method with  $N_r$  grid points is employed. The discretized equations are evolved in time using an implicit-explicit scheme, with the non-linear terms handled explicitly. For most of our simulation runs, we use a maximum spherical harmonic degree and order of  $\ell_{\max} = m_{\max} = 170$  and a radial resolution of  $N_r = 193$ . For the highest degrees of stratification explored, the spatial resolution is increased to  $\ell_{\max} = m_{\max} = 213$  and  $N_r = 321$ . These resolutions adequately resolve the characteristic radial and angular length scales of the instability both during the linear growth phase and throughout its nonlinear evolution, and ensure numerical convergence of the results, as consistently verified.

### 3.2. Initial condition and choice of dimensionless parameters

As initial condition for the magnetic field, we consider a purely axisymmetric azimuthal field of the form

$$\mathbf{B}(t=0) = \text{Lu}_0 r \sin \theta \hat{\boldsymbol{e}}_\phi, \quad (30)$$

which matches the background field profile used in the linear analysis of Sect. 2. In this study, we focus on the effect of gravity by varying the stratification parameter  $\delta_0$  from 0 (unstratified flow) to 900. The remaining parameters are set to  $\text{Lu}_0 = 2455$ ,  $\text{Pr} = 10^{-2}$ , and  $\text{Pm} = 1$ . The value of  $\text{Lu}_0$  is approximately 70 times larger than the critical value required for the onset of the Taylor instability in the unstratified case  $\delta_0 = 0$ .

Due to electron degeneracy, the Prandtl number  $\text{Pr}$  and the magnetic Prandtl number  $\text{Pm}$  are relatively high in red giant cores. Stellar evolution models suggest typical values of  $\text{Pr} \sim$

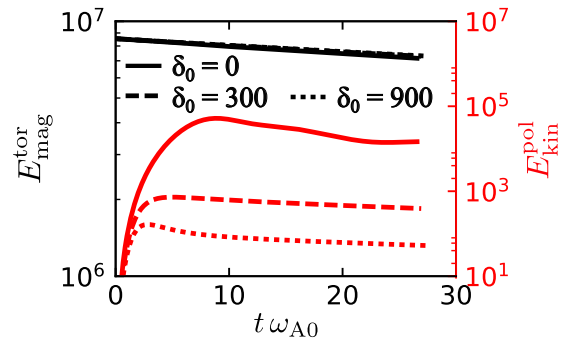


**Fig. 5.** Temporal evolution of the toroidal magnetic energy (black lines) and poloidal kinetic energy (red lines) for the unstratified run ( $\delta_0 = 0$ ) and for two stratified runs ( $\delta_0 > 0$ ). Note that the scales of the left and right vertical axes are different.

$10^{-3}$  (Garaud et al. 2015) and  $10^{-1} \lesssim \text{Pm} \lesssim 10$  (Rüdiger et al. 2015) for the degenerate cores of red giant branch stars with masses near that of the Sun. The value of  $\text{Pm}$  used in this study falls within these estimates, while  $\text{Pr}$  is only one order of magnitude larger.

Hereafter, we denote the azimuthal and meridional averages of an arbitrary function  $f(r, \theta, \phi, t)$  with angular brackets and an overbar respectively,

$$\langle f \rangle = \frac{1}{2\pi} \int_0^{2\pi} f d\phi \quad \text{and} \quad (31)$$

$$\bar{f} = \frac{1}{A} \int_0^\pi \int_{r_{\text{in}}}^{r_{\text{out}}} f r dr d\theta, \quad (32)$$

where  $A$  is the area of half the meridional plane. The non-axisymmetric components of the flow velocity and magnetic field are denoted by a prime. For example, the nonaxisymmetric magnetic field is given by  $\mathbf{B}' = \mathbf{B} - \langle \mathbf{B} \rangle$ .

### 3.3. Axisymmetric solutions

First, we examine the axisymmetric solutions obtained when varying stable stratification. The black lines in Fig. 5 illustrate the temporal evolution of the volume integrated toroidal magnetic energy  $E_{\text{mag}}^{\text{tor}} = \frac{1}{2} \int B_{\text{tor}}^2 dV$  for the unstratified run ( $\delta_0 = 0$ ),

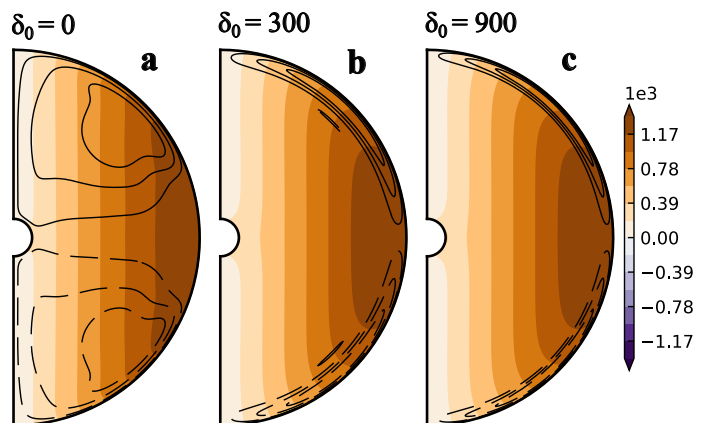


**Fig. 6.** Snapshots of the axisymmetric azimuthal field  $\langle B_\phi \rangle$  for the three runs shown in Fig. 5. The values of  $\delta_0$  are indicated at the top of each panel. The snapshot times  $t\omega_{A0}$  are 26.6, 24.5, and 27.3 respectively. Black contour lines represent the meridional circulation, with solid and dashed lines indicating clockwise and counterclockwise flows, respectively.

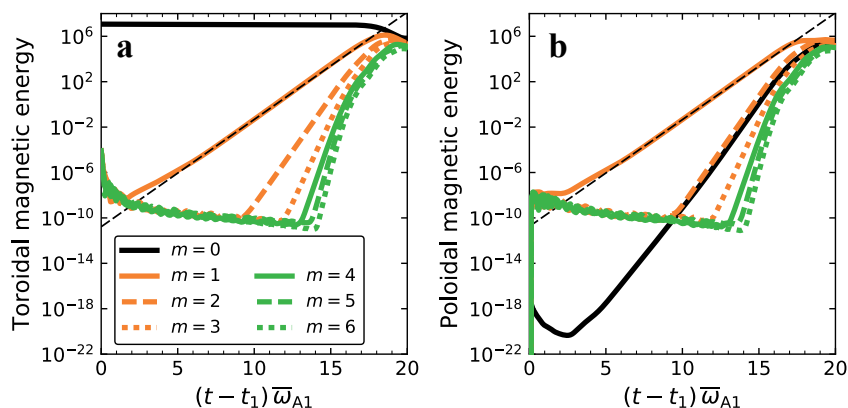


**Fig. 7.** Temporal evolution of the (a) toroidal and (b) poloidal magnetic energies of the azimuthal modes  $m = 0 - 6$  for the unstratified run TU0. The black dashed lines show exponential fits of the  $m = 1$  mode evolution within the period  $6.5 \leq (t - t_1) \bar{\omega}_{A1} \leq 10.5$ , providing the instability growth rates discussed in the text.

at an intermediate value of stable stratification ( $\delta_0 = 300$ ), and for highly stable stratification ( $\delta_0 = 900$ ). The magnetic field remains axisymmetric throughout its evolution and is purely toroidal, as no poloidal component is initialized in our simulations. Axisymmetric fields cannot be maintained by dynamo action (Cowling’s antidynamo theorem) and the toroidal field decays exponentially due to Ohmic diffusion as expected. As illustrated by the snapshots in Fig. 6, the axisymmetric azimuthal field,  $\langle B_\phi \rangle$ , preserves the cylindrical symmetry of the initial condition throughout its evolution, adjusting only at the spherical boundaries to satisfy the perfect conductor boundary conditions.

We observe an initial rapid growth of the poloidal kinetic energy  $E_{\text{kin}}^{\text{pol}} = \frac{1}{2} \int u_{\text{pol}}^2 dV$  (red lines in Fig. 5) driven by the development of meridional flows induced by the Lorentz force. These flows eventually relax into their end-state configuration after some Alfvén travel times. As expected, the amplitude of these flows decreases as  $\delta_0$  increases, since the restoring buoyancy force acts to prevent radial motions. In the unstratified run, the meridional flow exhibits a single large-scale circulation cell in each hemisphere (black isocontour lines in Fig. 6a). As stable stratification increases, the meridional flow becomes confined near the outer boundary, forming thin circulation cells that locally advect the azimuthal field (Fig. 6b,c). Over longer timescales, the amplitude of the meridional flows decays, following the behavior of the toroidal field and confirming their magnetic origin.

### 3.4. Stability to nonaxisymmetric perturbations

We investigate the stability of the axisymmetric solutions discussed in the previous section in response to weak nonaxisymmetric perturbations. The perturbations are introduced during the Ohmic decay phase of the evolution of the azimuthal field. They consist of a spatially uncorrelated, white noise that is added to the nonaxisymmetric ( $m > 0$ ) part of the spherical harmonic decomposition of the toroidal field. The root mean square (RMS) amplitude of the perturbations is typically 4 orders of magnitude lower than the one of the axisymmetric azimuthal field.

In the previous section, we demonstrated that the morphology of the axisymmetric azimuthal field shows only mild variations with the stratification parameter  $\delta_0$ . However, its amplitude decreases over time. We therefore define a local version of the stratification parameter at the perturbation time  $t = t_1$ ,

$$\delta_1 = \frac{N}{\omega_{A1}}, \quad (33)$$

where  $\omega_{A1} = B_{\phi 1}^*/(\mu\rho)^{1/2} r_0$  is the Alfvén frequency of the azimuthal field at the perturbation time  $B_{\phi 1}^* = B_\phi^*(r, \theta, t = t_1)$ . The parameter  $\delta_1$  exhibits an approximately cylindrical symmetry, with some modulations introduced by the chosen Brunt-Väisälä frequency profile  $N$ , and decreases roughly as  $1/r^2 \sin \theta$  throughout the fluid domain. To characterize the degree of stable stratification at the perturbation time, we define a mean value of this parameter as  $\bar{\delta}_1 = \bar{N}/\bar{\omega}_{A1}$ , which is reported in Table 2 along with the perturbation times  $t_1$ . Similarly, the characteristic azimuthal field strength at the perturbation time is represented by the mean Lundquist number  $\bar{\text{Lu}}_1 = \bar{B}_{\phi 1}^* r_0 / (\mu\rho)^{1/2} \eta$ , which can be interpreted as the ratio of the mean Alfvén frequency  $\bar{\omega}_{A1}$  to the magnetic diffusion rate  $\omega_\eta = \eta/r_0^2$ . The field strength at perturbation time is virtually fixed in our runs since  $\bar{\text{Lu}}_1$  ranges between 677 and 682 (Table 2).

In the following sections, we examine the linear evolution of the instability, starting with the unstratified case and then considering the effect of stratification.

#### 3.4.1. Unstratified flow

We start by examining the unstratified run from Sect. 3.3, and introduce the nonaxisymmetric perturbations at time  $t_1 = 26.6 \omega_{A0}^{-1}$  when  $\bar{\text{Lu}}_1 = 677$  (referred to as run TU0 hereafter). Figure 7 shows the temporal evolution of the toroidal and poloidal magnetic energies for the azimuthal modes  $m = 0$  to  $m = 6$  in this run. Approximately  $2/\bar{\omega}_{A1}$  after the perturbation time, the first mode to grow exponentially is  $m = 1$ , as expected for the Tayler instability. The linear growth rate of the RMS toroidal field associated to this mode is  $\sigma_{m=1} = 1.1 \bar{\omega}_{A1}$ , when evaluated in the period  $(t-t_1) \bar{\omega}_{A1} = 6.5 - 10.5$  (dashed black line in Fig. 7a). This value closely matches the rate calculated from the evolution of the  $m = 1$  poloidal field (solid orange line in Fig. 7b). The background axisymmetric ( $m = 0$ ) azimuthal field decays slowly due to Ohmic diffusion, with its evolution appearing nearly stationary during the linear growth phase of the instability (solid black line in Fig. 7a).

As expected, snapshots of the latitudinal field fluctuations  $B'_\theta$  during the linear phase of the instability growth reveal a distinct  $m = 1$  azimuthal symmetry (Fig. 8a,b). All the other nonaxisymmetric field and flow components exhibit the same symmetry and are therefore not shown here. There is no azimuthal drift of the nonaxisymmetric flow and field components, as expected in the absence of rotation (e.g., Rüdiger et al. 2012). The instability re-



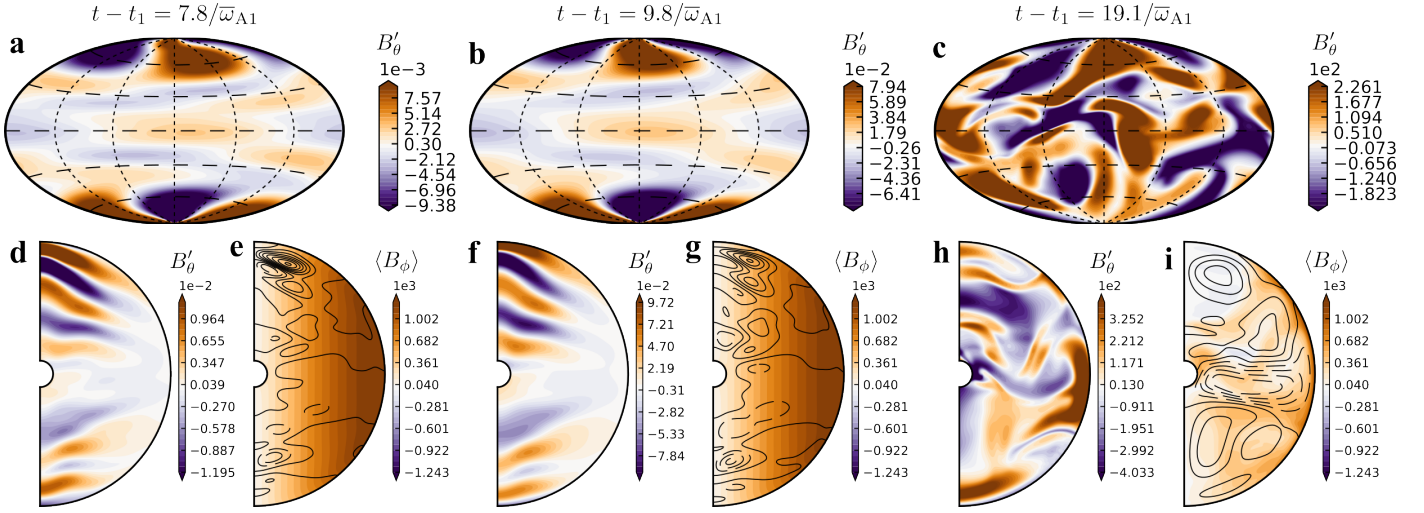


**Fig. 8.** Snapshots of the instability and axisymmetric field solution (a,d,e) during the linear phase of the instability evolution, (b,f,g) at the end of the linear phase, and (c,h,i) in the nonlinear stage for the unstratified run TU0. (a,b,c) Hammer projections of  $B'_\theta$  at radius  $r/r_{\text{out}} = 0.7$ . (d,f,h) Meridional cuts of  $B'_\theta$  at longitude  $\phi = 90^\circ$ . (e,g,i) Color isocontours show the axisymmetric azimuthal field and the superimposed black isocontour lines the axisymmetric poloidal field.

mains stationary also in the vertical direction and predominantly localizes in a wedge-shaped region around the vertical symmetry axis (Fig. 8d,f). This behavior aligns with predictions from our linear analysis, which indicates that the growth rates of the unstable eigenmodes decrease with the colatitude  $\theta$ , and is also consistent with classical results obtained from local linear stability studies in spherical geometry (Goossens & Tayler 1980). Our linear analysis also indicates that the characteristic radial wavenumber of the instability increases from the equator towards higher latitudes (black lines in Fig. 1), which qualitatively matches the structure of the instability in run TU0. We refrain from making a direct quantitative comparison between the numerical simulation results and the linear analysis due to the limitations inherent in the latter's approximations. In particular, the linear analysis may become questionable at higher latitudes near the symmetry axis, where the local approximation in the latitudinal direction is only partially satisfied. Additionally, the linear analysis neglects viscous and resistive effects, which would certainly influence the spectrum of the unstable radial modes if they were included. Finally, we note that the structure of the instability discussed above closely resembles that observed in global numerical studies of the Tayler instability in cylindrical geometry, which utilize the same background azimuthal field configuration as employed here (Rüdiger et al. 2012; Ji et al. 2023).

Figure 7 shows that modes  $m > 1$ , as well as the axisymmetric poloidal field (black line in the right panel), are subcritical initially. They begin to grow only at times  $t - t_1 \approx 10/\bar{\omega}_{A1}$ , as a result of nonlinear energy transfer from the large-amplitude  $m = 1$  mode. A simple weakly nonlinear analysis of the ideal induction equation by Ji et al. (2023) predicts that the nonlinear growth rates of the  $m = 0$  and  $m = 2$  modes are  $2\sigma_{m=1}$ . Higher chains of nonlinear interaction provide a nonlinear growth rate of  $m\sigma_{m=1}$  for modes  $m > 2$ . Figure 7b demonstrates that the nonlinear growth of the  $m = 0$  and  $m = 2$  poloidal field occurs at the same rate of  $2.2\bar{\omega}_{A1}$ , which is twice the rate of the  $m = 1$  mode, as anticipated. The nonlinear growth rates of the higher order modes in Fig. 7 are also in good agreement with the weakly nonlinear theory predictions. For simplicity, we hereafter denote the growth rate of the  $m = 1$  mode as  $\sigma$ .

The instability shows an apparent saturation at  $t - t_1 \approx 18/\bar{\omega}_{A1}$  when the nonaxisymmetric toroidal energy reaches val-

ues comparable to those of the background azimuthal field (Fig. 7a), with the nonaxisymmetric poloidal and toroidal energies roughly in equipartition. The field solution loses its simple azimuthal symmetry and transitions into a turbulent state, characterized by small-scale structures in the meridional plane (Fig. 8c,h). In this nonlinear stage, the axisymmetric field relaxes into a mixed poloidal-toroidal configuration (Fig. 8i), which no longer exhibits instability and slowly decays by resistive effects, along with the instability fluctuations. A detailed characterization of the nonlinear behavior of the instability is beyond the scope of this work and will be addressed in a future study. In the following section, we focus on the effect of stable stratification on the linear properties of the instability.

### 3.4.2. Effect of stable stratification

We now turn to investigate the impact of stable stratification on the linear properties of the instability. In our simulation runs, the mean stratification parameter  $\bar{\delta}_1$  ranges between 3.5 and 321 (see Table 2). In all stratified runs, similar to the unstratified case discussed above, the first azimuthal mode to grow exponentially after introducing the perturbations is  $m = 1$ . Higher modes exhibit dynamical evolutions analogous to those observed in run TU0

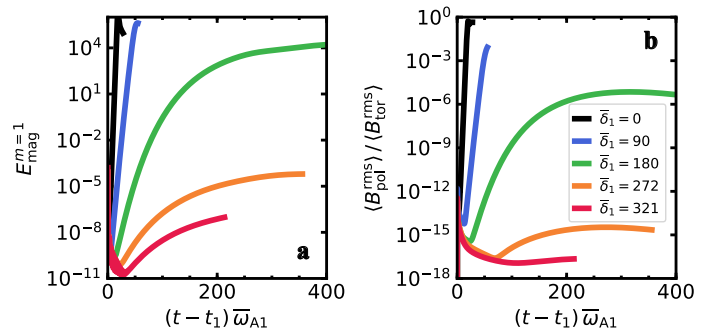


**Fig. 9.** Temporal evolution of the (a) magnetic energy of the azimuthal mode  $m = 1$ ,  $E_{\text{mag}}^{m=1}$ , and of the (b) axisymmetric poloidal to toroidal magnetic field ratio,  $\langle B_{\text{pol}}^{\text{RMS}} \rangle / \langle B_{\text{tor}}^{\text{RMS}} \rangle$ , for different values of the stratification parameter  $\bar{\delta}_1$ .

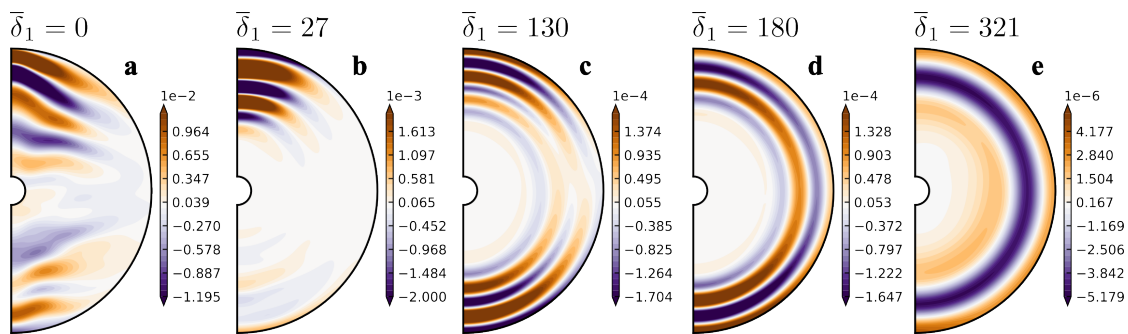
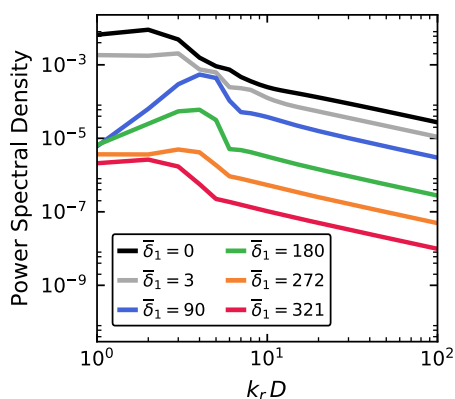


**Fig. 10.** Meridional cuts of  $B_\theta$  during the linear phase of the instability growth in 5 runs at different values of the stratification parameter  $\bar{\delta}_1$ . The leftmost panel shows the unstratified run TU0 discussed in Sect. 3.4.1.

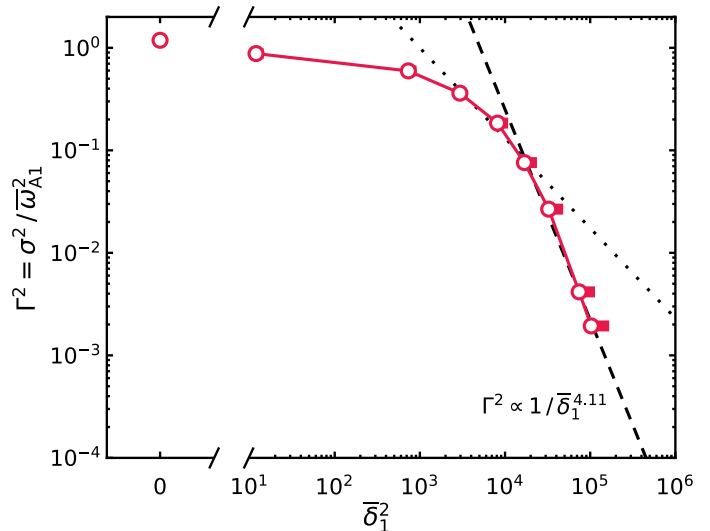
and are therefore not discussed further. The linear growth rate of the  $m = 1$  mode decreases rapidly as  $\bar{\delta}_1$  increases, as shown by the temporal evolution of the magnetic energy associated to this mode in Fig. 9a. The growth rates  $\sigma$ , presented in Table 2, range from  $0.94 \bar{\omega}_{A1}$  for the weakly stratified run at  $\bar{\delta}_1 = 3.5$  to values smaller by nearly two orders of magnitude in the most stratified run at  $\bar{\delta}_1 = 321$ . Significant variations of the growth rate with stratification were already observed in our linear analysis for the most unstable equatorial eigenmodes (Sect. 2.2.2).

Figure 9b displays the temporal evolution of the ratio of the RMS axisymmetric poloidal to toroidal field,  $\langle B_{\text{pol}}^{\text{RMS}} \rangle / \langle B_{\text{tor}}^{\text{RMS}} \rangle$ , evaluated over the entire fluid domain, for increasing stratification. In the unstratified run, as anticipated in the previous section, the instability fluctuations generate a strong axisymmetric poloidal field, so that the field ratio reaches a relatively high maximum value of 0.53, before decaying together with the instability fluctuations (black line). The field ratio systematically decreases with increasing stratification. For moderate stratification, its maximum value is only about 0.01 in run TS4 at  $\bar{\delta}_1 = 90$  (blue line), and becomes negligible in the runs with  $\bar{\delta}_1 \geq 180$ .

By limiting radial displacements, stable stratification influences the structure of the instability in the radial direction. Already for a weak stratification of  $\bar{\delta}_1 = 27$ , we observe a sizable decrease in the characteristic radial wavelength of the flow and field fluctuations compared to the unstratified run (Fig. 10a,b). The radial wavelength continues to decrease up to run TS5 at  $\bar{\delta}_1 = 130$  (Fig. 10c) and then increases for larger values of



**Fig. 11.** Fourier power spectral density of the latitudinal magnetic field fluctuations  $B_\theta$  along the radial coordinate for  $\theta = 45^\circ$  during the linear phase of the instability growth in 6 runs at different  $\bar{\delta}_1$  (see the legend inset). The power spectrum is averaged over all longitudes. The radial wavenumber  $k_r$  is in units of the shell gap  $D$ .



**Fig. 12.** Square of the normalized instability growth rate  $\Gamma$  as a function of  $\bar{\delta}_1^2$ . The dashed line shows the best-fit power law  $\Gamma^2 \propto 1/\bar{\delta}_1^{4.11}$  derived from the simulation data points in the highly stratified regime where  $\bar{\delta}_1^2 > 10^4$ . The dotted line displays the power law fit  $\Gamma^2 \propto 1/\bar{\delta}_1^{1.76}$  for the moderately stratified regime, which covers  $10^3 < \bar{\delta}_1^2 < 2 \times 10^4$ . The horizontal error bars indicate the variation of the stratification parameter  $\bar{\delta}_1$  during the linear evolution of the instability (see text for details). For the unstratified case and the first three less stratified runs, the error bars are smaller than the data point symbols themselves.

the stratification parameter (Fig. 10d,e). This is confirmed by a Fourier analysis of the radial profiles of  $B_\theta$ , taken at colatitude  $\theta = 45^\circ$  and performed over all longitudes. Figure 11 shows that the radial wavenumber corresponding to the peak of the (azimuthally averaged) Fourier power spectrum,  $k_r^{\text{max}}$ , increases with stratification up to  $4 D^{-1}$  (run TS5, green line) and then systematically lowers down to  $2 D^{-1}$  for the most stratified run TS7 at  $\bar{\delta}_1 = 321$  (red line). It is interesting to note that in the regime of highly stable stratification  $\bar{\delta}_1 \geq 180$ , most of the power is concentrated at low wavenumbers  $k_r \lesssim 7 D^{-1}$ . The large-scale radial structure of the instability fluctuations is evident in the snapshots shown in Fig. 10d,e, which also demonstrate that these fluctuations are nearly constant in latitude.

These findings are consistent with those obtained for the distributed equatorial eigenmodes in the linear analysis (Sect. 2.2.2). These eigenmodes, characterized by only a few radial nodes and distributed predominantly in the outer half of the radial fluid domain, closely resemble the morphology of the global modes observed in the numerical simulations. As stratifi-

cation increases from moderate to strong, we found a decrease in the characteristic radial wavenumber of the distributed equatorial eigenmodes – a trend also evident in the simulations. The linear analysis also captured the tendency of the instability fluctuations to align with equipotential gravity surfaces under stronger stratification (cf. Fig. 2).

Finally, we explore how the instability growth rate varies with stratification. Figure 12 presents the square of the normalized growth rate,  $\Gamma^2 = \sigma^2/\bar{\omega}_{A1}^2$ , as a function of  $\bar{\delta}_1^2$  for all our simulation runs. Here  $\sigma$  is calculated from the temporal evolution of the volume averaged toroidal magnetic energy associated to the  $m = 1$  mode, as described in Sect. 3.4.1. For  $\bar{\delta}_1^2 \lesssim 10^3$ , where stratification is weak, the growth rate only slightly decreases from the adiabatic value  $\Gamma \approx 1$  observed in the unstratified run. For intermediate stratification values,  $10^3 < \bar{\delta}_1^2 < 2 \times 10^4$ , stronger variations are apparent. A power law fit  $\Gamma^2 = c \bar{\delta}_1^{-2b}$  of the three simulation data points in this range yields  $c = 433$  and an exponent  $b = -0.88$  and is shown as a dotted line in Fig. 12. The value of  $b$  is close to the one found in the numerical simulations of Guerrero et al. (2019), which is  $-0.95$ . In the very stably stratified regime, where  $\bar{\delta}_1^2 > 10^4$ , the best fitting parameters are  $c = 4.07 \times 10^7$  and  $b = -2.05$  (dashed line). This latter value of  $b$  is in excellent agreement with the prediction by BU12, also confirmed by our linear analysis in Sect. 2.2.2. In this regime, the instability grows at such a slow rate that the amplitude of the background axisymmetric field  $\langle B_\phi \rangle$  decreases during the linear evolution of the instability, thereby leading to an increase in  $\bar{\delta}_1$  over time. The horizontal red lines in Fig. 12 show the values attained by  $\bar{\delta}_1$  during the linear phase of the instability growth and demonstrate that such variations do not impact the growth rate scaling. Our linear analysis suggested that the strong growth rate scaling in the regime of highly stable stratification is associated with the distributed equatorial eigenmodes, and that localized eigenmodes are unlikely to have a significant global dynamical impact on the system due to their local nature. The numerical simulation results seem to confirm this interpretation since we find no sign of localized unstable fluctuations neither at high latitudes nor in the equatorial region in this regime (Fig. 10d,e).

#### 4. Application to red giant cores

Our global linear analysis and direct numerical simulations confirm the relation of BU12 for the growth rate of the Tayler instability in strongly stably stratified spheres. When assuming the proportionality constant to be of order unity, Eq. (16) in BU12 is

$$\Gamma \approx \epsilon \delta^{-2} \quad (34)$$

or

$$\sigma \approx \frac{B_\phi^2 \kappa}{4\pi\rho R^4 N^2} \quad (35)$$

in dimensional (cgs) units, using the definitions in Sect. 2.2. For a given star, the knowledge of the size of its radiative region  $R$ , together with radial profiles of the density  $\rho$ , Brunt-Väisälä frequency  $N$ , and thermal diffusivity  $\kappa$  therein, allows us to predict a toroidal magnetic field strength necessary for developing instability with a characteristic growth time  $\sigma^{-1}$ . We denote the age of the radiative core forming after the main sequence phase by  $\tau$ . For  $\tau = \sigma^{-1}$ , Eq. (35) gives us a particular magnetic field

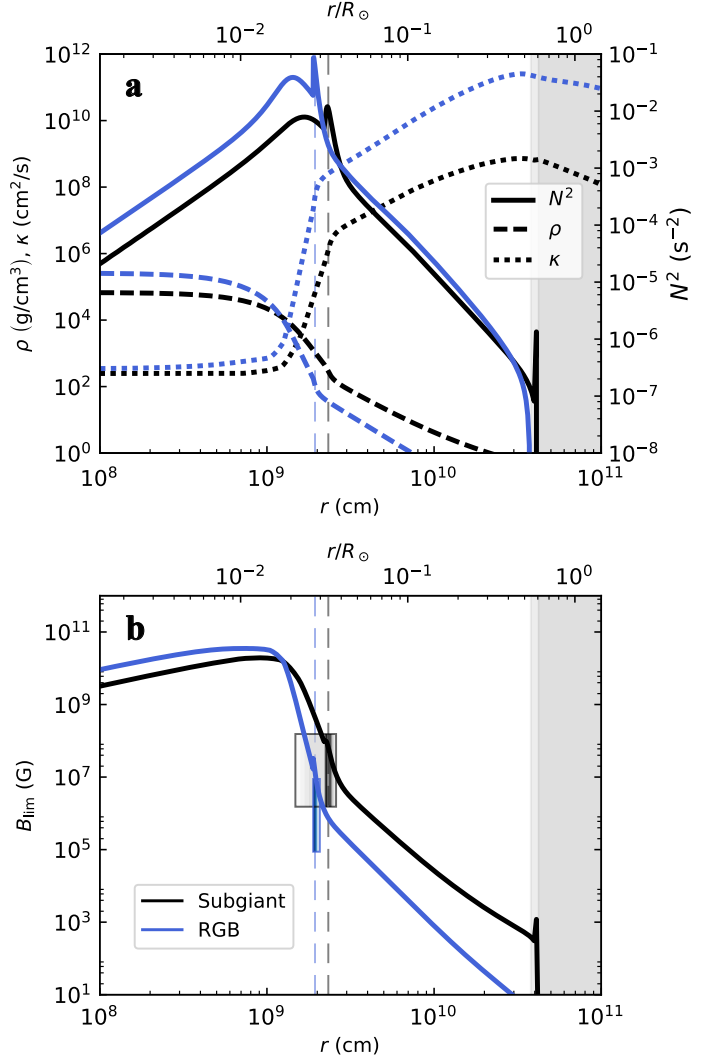


**Fig. 13.** Radial profiles of various quantities for the  $1.1 M_\odot$  stellar model in the subgiant (black) and red giant branch (blue) stages. (a) The squared Brunt-Väisälä frequency  $N^2$ , density  $\rho$ , thermal diffusivity  $\kappa$ , and (b) limiting unstable toroidal field  $B_{\text{lim}}$  are shown for the radiative cores and the lower part of the convection zones (grey shaded backgrounds) of the two stars. The approximate locations of the hydrogen burning shell are indicated by the dashed vertical lines. The rectangles in (b) indicate the range of estimated toroidal field strengths from the asteroseismic observations and their locations. The color contours within each rectangle show the weight function  $K(r)$  of the seismic inversions (see the text for more details). In each panel, the upper horizontal axis shows the radius  $r$  in units of the solar radius  $R_\odot$ . The surface radii of the subgiant and red giant are  $3.2$  and  $16.1 R_\odot$  respectively.

strength

$$B_{\text{lim}} = \frac{N (4\pi\rho)^{1/2} R^2}{(\tau\kappa)^{1/2}}. \quad (36)$$

For toroidal magnetic fields  $B_\phi < B_{\text{lim}}$ , the instability grows on timescales longer than  $\tau$ , and thus has negligible dynamical influence during the evolution period of the core. The instability produces a certain poloidal field which ultimately is the observable core magnetic field.

To estimate  $B_{\text{lim}}$ , we computed stellar evolution models of two stars with initial masses of  $1.1$  and  $1.5 M_\odot$ , which span the mass range of subgiants and red giants where internal magnetic fields have been detected (Sect. 1). Here  $M_\odot$  is the mass of the

Sun. The two stars were evolved with the Catania version of the Garching Stellar Evolution Code (Weiss & Schlattl 2008; Bonanno et al. 2002) from the zero age main sequence up to the red giant branch (RGB), with a final age of 10.53 and 3.34 Gyr for the 1.1 and 1.5  $M_{\odot}$  stars respectively. We assumed an initial hydrogen and helium mass fraction of  $X = 0.70$  and  $Y = 0.27$  respectively. No heavy-element diffusion was included and we chose a mixing-length parameter  $\alpha_{\text{MLT}} = 1.65$ , which is obtained from solar calibration. We choose two models for each mass, one in the subgiant (SG) phase and one at the base of the RGB. Since we did not find any significant difference in our estimates of  $B_{\text{lim}}$  for the two stellar masses, we discuss only the results for 1.1  $M_{\odot}$  in the following. The SG (RGB) model has an age of 10.127 (10.489) Gyr, radius  $R_*/R_{\odot} = 3.2$  (16.1) and luminosity  $L_*/L_{\odot} = 4.6$  (70.1), where  $R_{\odot}$  and  $L_{\odot}$  are the radius and luminosity of the Sun. We calculated the thermal diffusivity  $\kappa$  as (e.g., Cassisi et al. 2007)

$$\kappa = \frac{16 \sigma T^3}{3k\rho^2 c_p}, \quad (37)$$

where  $\sigma$  is the Stefan-Boltzmann constant,  $c_p$  is the specific heat capacity at constant pressure and  $k$  is the total opacity defined by  $k^{-1} = k_{\text{rad}}^{-1} + k_{\text{cond}}^{-1}$ , where  $k_{\text{rad}}$  and  $k_{\text{cond}}$  are, respectively, the radiative and conductive opacities calculated in GARSTEC (see Weiss & Schlattl 2008).

Figure 13a presents the radial profiles of the squared Brunt-Väisälä frequency  $N^2$ , density  $\rho$ , and thermal diffusivity  $\kappa$  in the radiative core and in the lower part of the convective envelope ( $N^2 < 0$ , grey shaded background) for the SG (black lines) and RGB (blue lines) stars. For each star, hydrogen burning takes place within a narrow shell, with its approximate location indicated by the vertical line marking the position of the luminosity jump, which roughly correlates with the peak in  $N^2$  (solid lines). The inner parts of the core below the hydrogen burning shell (HBS) are composed of inert helium. Below the HBS, the values of  $N^2$  increase by one order of magnitude from the SG to the RGB, due to an increase in density (dashed lines), which is a result of the core gravitational contraction. In these regions, where the plasma density reaches up to  $10^5 \text{ g/cm}^3$ , electron conduction is the dominant mechanism for heat transport. In contrast, in the core regions above the HBS, heat is primarily conducted by radiation. Due to the steep density decrease across the HBS, the thermal diffusivity  $\kappa$  (dotted lines) increases by more than 4 orders of magnitude from the inner degenerate regions of the core to the outer nondegenerate ones.

Figure 13b compares the radial profiles of the limiting unstable toroidal field  $B_{\text{lim}}$ , obtained from Eq. (36), with estimates of the toroidal field strengths  $B_{\phi}$  (shaded areas) obtained from the asteroseismic measurements of the radial magnetic fields  $B_r$ . These estimates are obtained as follows. Given that differential rotation likely exists in the outer parts of red giant cores (Deheuvels et al. 2014; Di Mauro et al. 2018), we can expect relatively strong toroidal fields, that is  $B_{\phi} \gtrsim B_r$ . On the other hand, the observed magnetic frequency splittings suggest that  $B_{\phi} \ll 10^2 B_r$  (Li et al. 2022; Deheuvels et al. 2023). Accordingly, we select a range of core toroidal field strengths such that  $1 \leq B_{\phi}/B_r \leq 10^2$ , which defines the vertical extent of the rectangles in Fig. 13b. In the 13 red giants where internal magnetic fields have been detected so far, the minimum measured RMS radial magnetic field strength,  $B_{r,\text{min}}$ , decreases with evolution from 609 kG to 35 kG (Deheuvels et al. 2023). The actual RMS radial field  $B_r$  can be higher, as the magnetic frequency splittings depend on a coefficient of order unity that encapsulates the

latitudinal distribution of the field, which cannot be determined from the asteroseismic observations (Li et al. 2022). When this coefficient is considered for a purely axisymmetric dipolar field, we obtain  $B_r = 2.5 B_{r,\text{min}}$ , which places the measured core radial field strengths at around 1.5 MG for young SGs and decreases to 88 kG on the RGB.

The radial field measurements just discussed probe a narrow region of the core around the HBS where the asteroseismic inversions are most sensitive. Specifically, the mixed mode frequency shifts depend on a weight function  $K(r) \propto (N/r)^3/\rho$ , which probes the gravity mode cavity and sharply peaks around the HBS (Li et al. 2022; Deheuvels et al. 2023). In Fig. 13b, the horizontal width of the rectangles covers the range  $[0.1 K_{\text{max}}, K_{\text{max}}]$ , where  $K_{\text{max}}$  is the maximum of the weight function, while the color contours indicate  $K(r)$  itself.

Figure 13b shows that in the core regions near and above the HBS, the limiting unstable toroidal field strength  $B_{\text{lim}}$  decreases as the star evolves from the SG phase to the RGB. These predicted limiting fields align well with the core toroidal fields estimated from the observations. These results indicate that the locally observed internal magnetic fields are compatible with toroidal fields that remain unstable throughout the evolution of red giant radiative cores. In contrast, in the degenerate regions of the core below the HBS,  $B_{\text{lim}}$  reaches extremely high values of about  $10^4$  MG, suggesting that toroidal fields in these inner parts of the core are likely stable.

## 5. Summary and conclusions

We explored the current-driven nonaxisymmetric ( $m = 1$ ) Tayler instability in a spherical domain using a linear, nonlocal stability analysis that incorporates the effects of a stably stratified background and thermal diffusivity. The analysis builds upon the one of Bonanno & Urpin (2012) by relaxing assumptions on the latitudinal structure of the background toroidal field. The chosen background toroidal field is in magnetohydrostatic equilibrium, where gravitational, pressure, and Lorentz forces are in balance as expected in radiative stellar interiors. The analysis delivers the global radial structure of the unstable  $m = 1$  perturbations, a feature inaccessible to classical fully local approaches (Acheson & Gibbons 1978; Spruit 1999; Skoutnev & Beloborodov 2024), and highlights the role of gravity in mitigating these perturbations.

We employed the same background toroidal field to study the Tayler instability using 3D direct numerical simulations in a nearly full-sphere geometry, tracking the evolution of the instability from the linear to the nonlinear phase. In contrast to previous numerical studies in spherical geometry, our simulations include the effects of viscosity and magnetic resistivity, and explore a regime of highly stable stratification that has not been reached in prior work (Guerrero et al. 2019).

Both the linear analysis and the numerical simulations demonstrate that gravity exerts a strong stabilizing effect on the Tayler instability. As the stratification parameter  $\delta$ , defined as the ratio of the Brunt-Väisälä frequency  $N$  to the Alfvén frequency of the background toroidal field  $\omega_{A0}$ , increases, the linear analysis shows that the most unstable modes become confined in regions around the poles. In the regime of strong stable stratification characteristic of stellar interiors ( $\delta \gg 1$ ), these high-latitude modes are highly localized near the poles and are characterized by small radial length scales, which suggests that their global dynamical impact on the system is negligible. The dynamics is then dominated by the large-scale modes that develop at low latitudes and that grow at a reduced rate because of the strong stabilizing



effect of gravity, which is nearly antiparallel to the unstable motions in this region. We find that the dimensionless growth rate of the low-latitude modes follows a scaling of  $\Gamma \sim \delta^{-2}$ , or equivalently, in dimensional quantities,  $\sigma \sim N^{-2}\omega_{A0}^3$ , as anticipated by BU12. We note that fully local analyses of the Tayler instability generally focus on a location near the poles and hence miss the stabilizing effect of gravity substantially.

For sufficiently strong stratification, our numerical simulations provide clear confirmation of the above scaling for the first time. As in the linear analysis, the unstable flow and magnetic field fluctuations in the highly stratified regime are large scaled, exhibiting only a few radial nodes and remaining nearly constant in the latitudinal direction. In this regime, the field fluctuations grow so slowly that the background axisymmetric toroidal field strength ( $B_{\text{tor}}^{\text{RMS}}$ ) starts to decay by resistive effects before the nonlinear stage is reached and the axisymmetric poloidal field ( $B_{\text{pol}}^{\text{RMS}}$ ) generated by the instability remains negligible. While a detailed characterization of the nonlinear solutions is reserved for future work, our simulations suggest that the magnetic fields in the highly stratified regime adopt simple large-scale axisymmetric geometries dominated by the toroidal component. Conversely, in the unstratified and weakly stratified runs, the instability alters the initial axisymmetric toroidal field, producing turbulent field solutions that exhibit a mixed toroidal-poloidal character.

Our results open the possibility to better understand where in radiative stellar interiors and when in stellar evolution magnetic fields may remain stable for considerable amounts of time. We computed stellar evolution models for a  $1.1 M_{\odot}$  star and selected two evolutionary stages: the early subgiant phase and the base of the RGB. The models provide radial profiles of the Brunt-Väisälä frequency  $N$ , density  $\rho$ , and thermal diffusivity  $\kappa$  in the radiative core. Using the growth rate scaling from BU12,  $\Gamma \approx \epsilon \delta^{-2}$ , we estimated the limiting toroidal field strength  $B_{\text{lim}}$  for which the growth time of the Tayler instability matches the typical core evolution timescale. Unstable toroidal fields  $B_{\phi} < B_{\text{lim}}$  evolve on longer timescales and cannot play a role in the internal core dynamics. In the outer, non-degenerate parts of the core, we find that  $B_{\text{lim}}$  decreases from the subgiant to the RGB phases. Specifically, near the hydrogen burning shell, its value declines from  $10^2$  to  $10 \text{ MG}$  throughout these two evolutionary stages. These values align with the expected toroidal field strengths in this region, which we estimated from the available asteroseismic radial magnetic field measurements (Li et al. 2022; Deheuvels et al. 2023). This agreement suggests that the Tayler instability may influence the dynamics of the outer parts of red giant cores. In contrast, in the degenerate parts of the core below the HBS,  $B_{\text{lim}}$  is as high as  $10^4 \text{ MG}$ , indicating that these regions most likely harbor stable toroidal fields.

In this study, we did not investigate the effect of rotation on the instability, leaving this for future work. Local linear perturbation theory, however, suggest that the Coriolis force reduces the instability growth rate compared to the nonrotating case (Pitts 1985; Spruit 1999; Skoutnev & Beloborodov 2024). A comprehensive understanding of the Tayler instability and the resulting turbulent transport under the combined influences of rotation, differential rotation, and strong stable stratification – conditions relevant to stellar interiors – remains incomplete. Current numerical studies consider only weakly stratified flows (Petitdemange et al. 2023; Barrère et al. 2023), while estimates of the turbulent transport rely heavily on results from local stability analyses valid near the poles (Spruit 2002; Fuller et al. 2019). Extending numerical simulations to highly stratified regimes, as initiated in this work, alongside nonlocal linear analyses like the one per-

formed, is crucial for accurately quantifying the turbulent transport induced by the Tayler instability and the eventual associated dynamo mechanism.

*Acknowledgements.* This research was funded by the Deutsche Forschungsgemeinschaft (DFG, German Research Foundation) – AR 355/13-1, within the framework of “Stability and generation of magnetic fields in red giants: towards a unified picture”. AB acknowledges support from the European Union – NextGenerationEU RRF M4C2 1.1 n: 2022HY2NSX “CHRONOS: adjusting the clock(s) to unveil the CHRONO-chemo-dynamical Structure of the Galaxy” and from the research grant “Unveiling the magnetic side of the Stars” funded under the INAF national call for Fundamental Research 2023.

## References

- Acheson, D. J. & Gibbons, M. P. 1978, *Philosophical Transactions of the Royal Society of London Series A*, 289, 459
- Arlt, R. & Rüdiger, G. 2011, *Astronomische Nachrichten*, 332, 70
- Balbus, S. A. 1995, *ApJ*, 453, 380
- Barrère, P., Guilet, J., Raynaud, R., & Reboul-Salze, A. 2023, *Monthly Notices of the Royal Astronomical Society: Letters*, 526, L88
- Bhattacharya, S., Das, S. B., Bugnet, L., Panda, S., & Hanasoge, S. M. 2024, *ApJ*, 970, 42
- Bonanno, A., Schlattl, H., & Paternò, L. 2002, *A&A*, 390, 1115
- Bonanno, A. & Urpin, V. 2008a, *A&A*, 488, 1
- Bonanno, A. & Urpin, V. 2008b, *A&A*, 477, 35
- Bonanno, A. & Urpin, V. 2011, *Phys. Rev. E*, 84, 056310
- Bonanno, A. & Urpin, V. 2012, *ApJ*, 747, 137
- Braithwaite, J. & Nordlund, Å. 2006, *A&A*, 450, 1077
- Cassisi, S., Potekhin, A. Y., Pietrinferni, A., Catelan, M., & Salaris, M. 2007, *ApJ*, 661, 1094
- Christensen, U. R. & Wicht, J. 2007, in *Core Dynamics*, ed. G. Schubert, Vol. 8 (Elsevier), 245–282
- Deheuvels, S., Doğan, G., Goupil, M. J., et al. 2014, *A&A*, 564, A27
- Deheuvels, S., Li, G., Ballot, J., & Lignières, F. 2023, *A&A*, 670, L16
- Di Mauro, M. P., Ventura, R., Corsaro, E., & Lustosa De Moura, B. 2018, *ApJ*, 862, 9
- Duez, V., Braithwaite, J., & Mathis, S. 2010, *ApJ*, 724, L34
- Freidberg, J. P. 1970, *Physics of Fluids*, 13, 1812
- Fuller, J., Cantiello, M., Stello, D., Garcia, R. A., & Bildsten, L. 2015, *Science*, 350, 423
- Fuller, J., Piro, A. L., & Jermyn, A. S. 2019, *MNRAS*, 485, 3661
- Garaud, P., Medrano, M., Brown, J. M., Mankovich, C., & Moore, K. 2015, *ApJ*, 808, 89
- Gilman, P. A. 1970, *ApJ*, 162, 1019
- Goedbloed, J. P. & Hagebeuk, H. J. L. 1972, *Physics of Fluids*, 15, 1090
- Goossens, M. & Tayler, R. J. 1980, *MNRAS*, 193, 833
- Guerrero, G., Del Sordo, F., Bonanno, A., & Smolarkiewicz, P. K. 2019, *MNRAS*, 490, 4281
- Ji, S., Fuller, J., & Lecoanet, D. 2023, *MNRAS*, 521, 5372
- Jouve, L., Gastine, T., & Lignières, F. 2015, *A&A*, 575, A106
- Jouve, L., Lignières, F., & Gaurat, M. 2020, *A&A*, 641, A13
- Kaufman, E., Lecoanet, D., Anders, E. H., et al. 2022, *MNRAS*, 517, 3332
- Kitchatinov, L. & Rüdiger, G. 2008, *A&A*, 478, 1
- Knobloch, E. 1992, *MNRAS*, 255, 25P
- Li, G., Deheuvels, S., Ballot, J., & Lignières, F. 2022, *Nature*, 610, 43
- Li, G., Deheuvels, S., Li, T., Ballot, J., & Lignières, F. 2023, *A&A*, 680, A26
- Meduri, D. G., Jouve, L., & Lignières, F. 2024, *A&A*, 683, A12
- Monteiro, G., Guerrero, G., Del Sordo, F., Bonanno, A., & Smolarkiewicz, P. K. 2023, *MNRAS*, 521, 1415
- Parker, E. N. 1966, *ApJ*, 145, 811
- Petitdemange, L., Marcotte, F., & Gissinger, C. 2023, *Science*, 379, 300
- Pitts, E. and Tayler, R. J. 1985, *Monthly Notices of the Royal Astronomical Society*, 216, 139
- Prendergast, K. H. 1956, *ApJ*, 123, 498
- Rüdiger, G., Gellert, M., Schultz, M., et al. 2012, *ApJ*, 755, 181
- Rüdiger, G., Gellert, M., Spada, F., & Tereshin, I. 2015, *A&A*, 573, A80
- Schaeffer, N. 2013, *Geochemistry, Geophysics, Geosystems*, 14, 751
- Skoutnev, V. A. & Beloborodov, A. M. 2024, *arXiv e-prints*, arXiv:2404.19103
- Spruit, H. C. 1999, *A&A*, 349, 189
- Spruit, H. C. 2002, *A&A*, 381, 923
- Szklarski, J. & Arlt, R. 2013, *A&A*, 550, A94
- Tayler, R. J. 1973, *MNRAS*, 161, 365
- Velikhov, E. P. 1959, *Soviet Journal of Experimental and Theoretical Physics*, 9, 995
- Weiss, A. & Schlattl, H. 2008, *Ap&SS*, 316, 99
- Wicht, J. 2002, *Physics of the Earth and Planetary Interiors*, 132, 281